Direct Torque Control for Cable Conduit Mechanisms for the Robotic Foot for Footwear Testing

Abstract

As the shoe durability is affected directly by the dynamic force/pressure between the shoe and its working environments (i.e., the contact ground and the human foot), a footwear testing system should replicate correctly this interaction force profile during gait cycles. Thus, in developing a robotic foot for footwear testing, it is important to power multiple foot joints and to control their output torque to produce correct dynamic effects on footwear. The cable conduit mechanism (CCM) offers great advantages for designing this robotic foot. It not only eliminates the cumbersome actuators and significant inertial effects from the fast-moving robotic foot but also allows a large amount of energy/force to be transmitted/propagated to the compact robotic foot. However, CCMs cause nonlinearities and hysteresis effects to the system performance. Recent studies on CCMs and hysteresis systems mostly addressed the position control. This paper introduces a new approach for modeling the torque transmission and controlling the output torque of a pair of CCMs, which are used to actuate the robotic foot for footwear testing. The proximal torque is used as the input signal for the Bouc-Wen hysteresis model to portray the torque transmission profile while a new robust adaptive control scheme is developed to online estimate and compensate for the nonlinearities and hysteresis effects. Both theoretical proof of stability and experimental validation of the new torque controller have been carried out and reported in this paper. Control experiments of other closed-loop control algorithms have been also conducted to compare their performance with the new controller effectiveness. Qualitative and quantitative results show that the new control approach significantly enhances the torque tracking performance for the system preceded by CCMs.

Index Terms

Torque mode control, footwear testing, hysteresis model, cable conduit mechanism, robust adaptive control.

1 Introduction

Flexible transmission mechanisms such as cable-conduit mechanism (CCM) and tendon-sheath mechanism (TSM) have been widely adopted and developed in many types of applications from surgical robots [1-4] to robotic hands [5, 6], wearable robots [7], and soft exosuits [8, 9]. A CCM (or a TSM) consists of a cable/tendon which goes through a flexible conduit/sheath and connects an actuator with the robotic joint. One end of the cable/tendon attaches to a proximal pulley, which is controlled by an actuator, while its other end connects to a distal pulley, which attaches to the robotic joint. The conduit/sheath is a flexible tube which lets the cable/tendon go through and can hold constant length so that the force/motion can be propagated from the proximal pulley to the distal pulley. Thus, these mechanisms allow designers to install the output joints away from the actuators and therefore are the preferred solutions for those systems requiring narrow working environments and tortuous transmission routes. They are also very suitable for those applications which require high payload, compact design, and small weight and inertia such as for rehabilitation [10], exoskeletons [11, 12], and ankle-foot prosthesis [13]. Utilizing these advantages, Nguyen *et al.* [14, 15] adopted the CCMs to develop a robotic foot for footwear testing.

This robotic foot was designed to simulate the wear conditions that the footwear encounters in different walking, running, and other sports gaits with various ground conditions so that the system can automatically evaluate the footwear designs in a realistic testing manner. It consists of three primary segments (i.e., the shank, the foot, and the toe) and two controlled joints (i.e., the ankle joint and the metatarsophalangeal (MTP) joint). To simulate correctly the wear conditions caused by the human foot, the robotic foot should have similar capacity to mimic the human foot biomechanics during gaits. In high dynamic gaits (e.g., high running gaits), the human foot's joints convey a very high amount of torque/energy during gait cycles [16-18]. Also, the robotic foot must have the same shape, size, and appearance of the human foot. Thus, available robotic feet with traditional transmissions [19-22] cannot afford adequate power to mimic high dynamic gaits. On the other hand, CCMs, which can tether-transmit the force/motion to the joints from remote actuators and have compact designs, are very suitable to develop a powered robotic foot. CCMs not only offer great power for the foot joints but also eliminate the high inertial effects caused by cumbersome motors and actuators out of the fast-moving robotic foot.

However, the other natural characteristics of CCMs and TSMs such as nonlinear friction and backlash hysteresis limit the system performances. These drawbacks are the results of the interactions between the cables and the conduits in operation, especially when the conduit configurations randomly change along with the movement of the output joint location. In those scenarios, high accuracy tracking control results are much more difficult to accomplish. There are two primary approaches to compensate the friction and backlash hysteresis effects of CCMs including (i) the feedforward friction compensation based on model parameters and off-line identification results without any real-time feedback during the operations, and (ii) the closed-

loop compensation in real-time with the aids of indirect sensors (because traditional sensors such as encoders and force transducers are often not applicable for applications of CCMs).

To improve the system performance without the output sensors (i.e., the off-line compensation methods), many research groups such as Tian and Wang [23], Phee *et al.* [24], Pali *et al.* [5], Chen *et al*. [25], and Wu *et al*. [26] have been developing the lumped mass element methods with Coulomb friction model to characterize the force/motion transmission of the TSMs. Subsequently, inverse models and control signals were derived to compensate the friction. Nevertheless, these approaches often require in advance the cable-conduit configurations and assume the uniform distribution of the cable pretension. These conditions are either difficult to achieve or not practical. Other limitations in these methods include the dramatic increase of computation when the users increase the number of lumped elements and the discontinuity phenomenon in control due to the use of the static Coulomb friction model. Furthermore, by employing a set of partial derivative equations, Agrawal *et al*. [27] are able to describe the TSM transmission characteristics without the assumption of constant pretension and the knowledge of sheath configuration. However, complex model parameters, computational burden, and discontinuity are still the common limitations of this approach. Another major approach in modeling the TSM and CCM transmission characteristics is the use of either the backlash models [28, 29] or the backlash-like hysteresis models [30-32] to capture the transmission profile. Subsequently, inverse models and feedforward control signal are derived to compensate the friction and backlash effects. Although the off-line compensation approaches do not require output feedback and thus suitable for those systems which cannot install any sensor at the joints, they cannot cope with the dramatic changes of the transmission characteristics when the pretension and cable-conduit configurations vary in operation. Therefore, they limit the tracking control performance. In addition, few studies on torque tracking control were found. Although Wu *et al.* [26] and Jeong *et al.* [33] carried out some experiments on torque tracking control, however, fixed configuration assumption and limited tracking performance are still their drawbacks.

Alternatively, by employing non-traditional and indirect sensors (e.g., image processing systems) to feed back the output, researchers can adopt closed-loop control algorithms to enhance the position tracking performance. Recently, Do *et al.* [34-36] adopted the Bouc-Wen model [37, 38] to describe the motion transmission with displacement input and developed adaptive control schemes to cope with the changes of the conduit configuration and track to the position reference. However, no force/torque control algorithm was proposed. In addition, in the art of control theory for systems with hysteresis and nonlinearities (e.g., mechanical actuators, electromagnetic fields, and electronic relay circuits), many studies [39-42], [43] have developed various control schemes to compensate for the backlash-like hysteresis effects. Nonetheless, few experimental validations have been conducted [43] and no force/torque control scheme was proposed.

On the other hand, to develop the robotic foot for footwear testing, it is crucial to control the output torque at the foot's joints in order to replicate correctly the wear conditions that the footwear endures during the gaits. Thus, our prime objective is to address the challenges of output torque tracking control. The database search on Elsevier's Scopus and ISI Web of Science with keywords such as cable conduit mechanism, tendon sheath mechanism, Bowden cable mechanism, and cable-driven control found few studies on force/torque control for those mechanisms. Although the cable-driven rotary series elastic actuator (RSEA) developed by Kong *et al.* [44] operates in torque mode control, the system only uses the position feedbacks and derived cable tensions to compensate the friction in four cases of the cable curvature. Similarly, Lu *et al.* [45] used the derived output torque from the distortion of the torsional spring, the off-line estimations of the geared motor's inertia and damping, and a disturbance observer (DOB) to control the zero output torque for a human assistive joint actuated by a cable-driven RSEA. In addition, for the system actuated by a single CCM, Zhang *et al.* [46] carried out a case study of nine low-level controllers and three high-level controllers in torque mode control to find the best control schemes for driving an ankle exoskeleton to assist the human ankle in walking. However, this system also used the feedback extension of the elastic element (i.e., the series spring) to derive the output torque and the none-modeled control laws to track to the reference torque profile regardless the nonlinear transmission characteristics of the CCM. By installing four vertical load cells at four corners and one horizontal load cell in front of the contact floor of the robotic footwear testing system, the authors can monitor the ground reaction forces and calculate the output torque at the foot's joints. Therefore, in this paper, we design a new robust adaptive control scheme for torque tracking with the availability of output torque feedback. A torque transmission model developed from Bouc-Wen hysteresis model and proximal input torque is used to compensate for hysteresis effect of the CCMs. Three conventional closed-loop controllers are also implemented and assessed their torque tracking performances.

The first novelty of this paper is a method of modeling the torque transmission of a pair of CCMs. Instead of using the proximal displacement as an input and then calculating friction forces on the CCMs in the well-known Bouc-Wen hysteresis model, this paper uses a measured proximal torque as the input for the Bouc-Wen model. Then, the output distal torque is expressed directly in term of the input proximal torque by the Bouc-Wen hysteresis model. This modeling method reduces the order of the system time-derivative equations and allows the authors to control the output torque which is independent of proximal displacement.

The second novelty is a new adaptive control design. In this design, an accumulative error is chosen as the variable of interest. Then, followed the design process, this accumulative error, the tracking error, and its first time-derivative are added to the torque control signal. This means that this adaptive controller does account for the tracking error, its changing speed, and its accumulation. Similar to the PID controller, this controller helps reduce steady-state error and overshoot while it can also estimate and compensate for system hysteresis to improve torque tracking performance. In addition, with the proposed Lyapunov

function, the authors can prove analytically that the torque tracking error converges to a small constant (in a robust adaptive control design with leakage σ-modifications).

2 Experimental System and Problem Formulation

2.1 Experimental System

To investigate the torque transmission characteristics of the CCMs and develop the torque control algorithms for the robotic foot's joints, we installed a 1-DOF robotic system actuated by a pair of CCMs as shown in Fig. 1. The mechanical system comprises four primary groups, the actuator, the pair of CCMs, the feedback sensors, and the loading mechanism. Firstly, the pair of CCMs consists of two pulleys (i.e., the proximal and distal pulleys) which are connected by two galvanized cables (provided by CarlStarhl GmbH, Germany). These are the same set of CCMs which is used to actuate the ankle joint of the robotic foot. The cable diameter is 2.5 mm. The conduit inner diameter is 3.0 mm and its outer diameter is 6.8 mm. Each end of the cable is firmly attached to the pulley by screws. Each conduit support is equipped with two hollow screws which allow the cables to go through, hold the flexible conduits, and adjust the cable pretension. Secondly, the feedback sensors include a high-resolution incremental encoder (i.e., the SCH50F-4096 from SCANCON, Denmark) installed at each pulley to monitor the proximal and distal angular displacements. However, the most important sensors are the high-accuracy torque sensors. A TRS300-100Nm (from Futek, Southern California) with the measurement capacity of 100Nm is installed at the distal pulley to feed back the output torque while a T8-ECO-200Nm (provided by Interface, UK) is used to monitor the input torque at the proximal pulley. Thirdly, the loading mechanism comprises of two high-stiffness tension springs connecting with a third pulley by two flexible loading cables. The other ends of the springs connect to a fixed frame. This frame holds the spring when it is in tension but allows it to go down when it is not so that the system does not experience any cable-spring slacking. Finally, the actuator consists of a 3-phase AC brushless servomotor (the 115U2D300BACAA130240 from Control Technique, Emerson) connecting with a zero-backlash gearbox (the GBPH-1202-NP-015 from Anaheim Automation) and couplings. The couplings are the high-stiffness zero-backlash couplings (provided by MISUMI, Japan), therefore, backlash hysteresis only occurs on the CCMs.

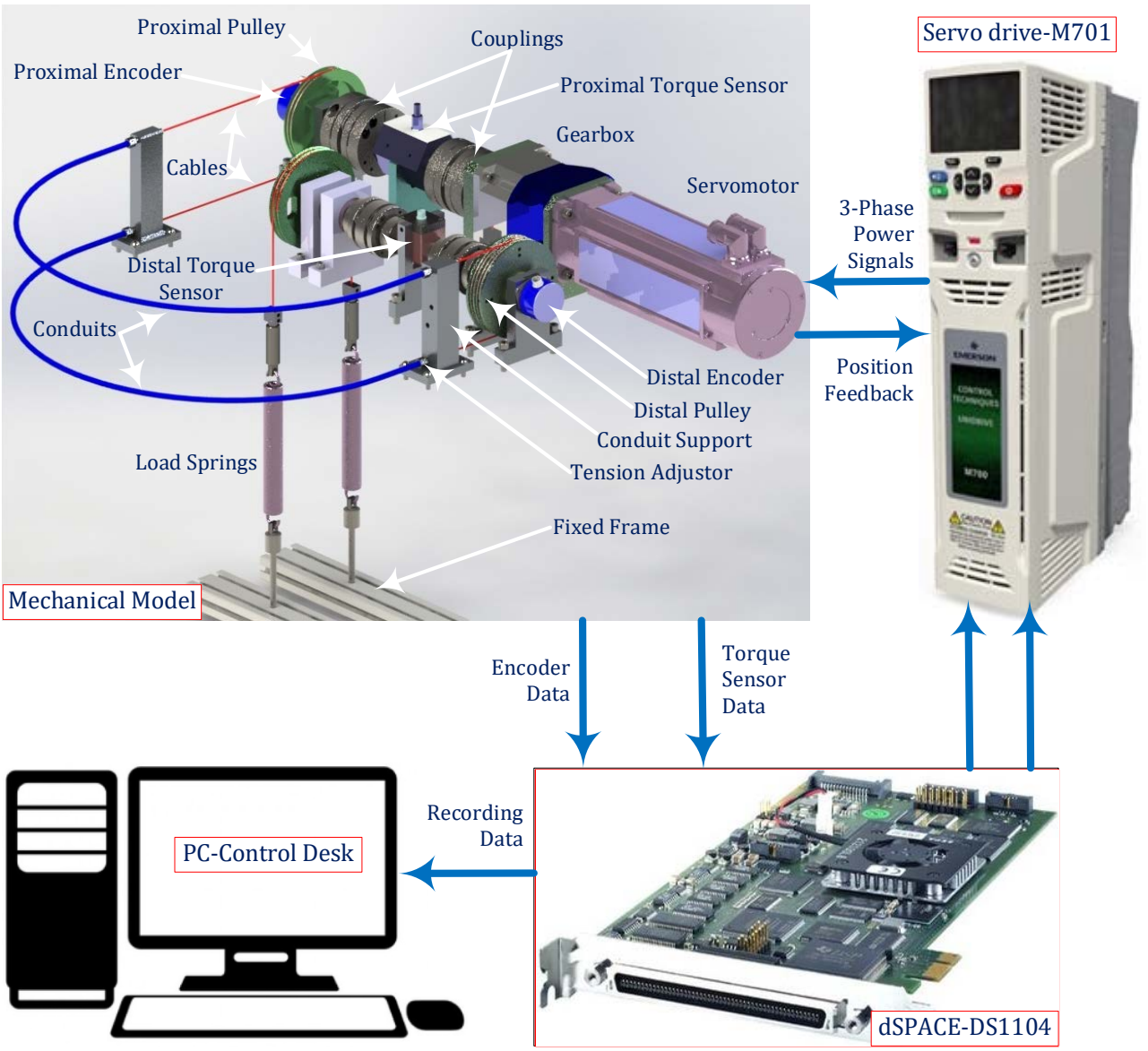

Fig. 1: The 1-DOF system actuated by a pair of cable-conduit mechanisms (CCMs)

The servomotor of the actuator is controlled by a servo drive M701-03400100A (from Control Technique, Emerson) which receives analog control signals from the real-time controller dSPACE DS1104. This controller receives all feedback signals from the sensors and calculates the control signals for the servo drive. It is installed in the computer PCI slot and send the monitoring signals simultaneously to the Control Desk to record the signals.

2.2 System Modelling

2.2.1 Transmission Characteristics of a pair of CCMs

The Bouc-Wen hysteresis model has been widely adopted in many mechanical systems to model the restoring force (or the friction) [38]. With displacement input x, the hysteresis friction can be modeled as

$$F(t) = k_x x + k_\eta \eta, \tag{1}$$

where k_x and k_η are positive coefficients, and η is the hysteresis internal state which can be derived by

$$\dot{\eta} = \rho[\dot{x} - \sigma|\dot{x}||\eta|^{n-1}\eta + (\sigma - 1)\dot{x}|\eta|^{n}]. \quad (2)$$

In this model, the positive parameters ρ, σ, and n control the shape of the hysteresis loop while k_x and k_η determine the amplitude of friction and the width of the hysteresis loop. Do *et al.* [30, 31, 34] also developed the Bouc-Wen model with proximal displacement input and an asymmetrical coefficient to estimate and compensate the friction of both single and pair of CCMs to control the distal output position. However, our target is to control the output torque. Also, since properties of the shoe and contact floor are the testing targets and wildly change during the tests, the impedance control laws based on displacement feedback is not applicable. Thus, the direct torque control is proposed for this system. Firstly, we are going to find the torque transmission characteristics from the proximal pulley to the distal pulley and compensate for the friction and hysteresis effects to enhance the torque tracking control performance. Fig. 2 shows an illustration of the transmission fundamentals of the pair of CCMs and loading mechanism.

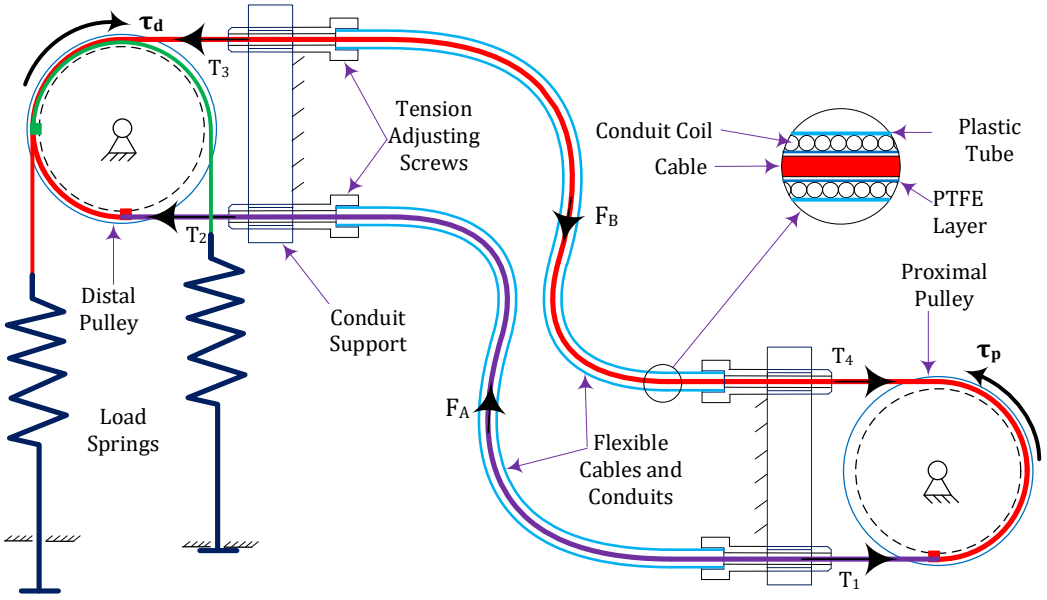

Fig. 2: The transmission principle of a pair of CCMs

Denote T_1, T_2 as the tensions at two ends of cable A and T_3, T_4 as the tensions at two ends of cable B, assume that two pulleys have the same radius r, one can obtain the following equation:

$$\tau_p(t) - \tau_d(t) = \tau_f(t), \quad (3)$$

where $\tau_p = r(T_1 - T_4)$ is the proximal torque, $\tau_d = r(T_2 - T_3)$ is the distal torque, and τ_f represents the total friction effect on both CCMs. Note that if two pulleys have different radii as r_1 and r_2, the proximal torque is $\tau_p = r_1(T_1 - T_4)$ and the distal torque is $\tau_d = r_2(T_2 - T_3)$. Then, adding two sides of $F_A = T_1 - T_2$ with $F_B = T_3 - T_4$, and multiplying the resulted equation with positive constant $r_1 r_2$ yields $\tau_p(t) - (r_1/r_2)\tau_d(t) = \tau_f(t)$, in which $\tau_f(t) = r_1(F_A + F_B)$ represents the equivalent friction torque.

In addition, the distal torque satisfies

$$\tau_d = kr^2\varphi_d + c_o\dot{\varphi}_d + (mr^2 + J_o)\ddot{\varphi}_d, \tag{4}$$

where φ_d, $\dot{\varphi}_d$, $\ddot{\varphi}_d$ are the angular displacement, velocity, and acceleration of the distal pulley; J_o, c_o are the total inertial and viscous coefficient of the distal pulley, couplings and loading pulley; τ_d is the distal torque; m is the mass of the spring and connectors; and k is the spring stiffness.

2.2.2 Transmission Observation, Modelling and Parameters Identification

To investigate the torque transmission characteristics of the pair of CCMs, we carried out numerous observation trials. Fig. 3 illustrates the block diagram of the observation process. From the digital to analog conversion (DAC) modules of the controller DS1104, a torque reference signal $\tau_r(t) = 0.144\sin(\pi t)$ and a maximum speed reference signal $v_{max}(t) = 0.3$ were sent to the servo drive, which was operating in torque mode control. This drive calculated the reference current $i_r(t)$ from the input signals (i.e., $\tau_r(t)$ and $v_{max}(t)$). It drove the servomotor to generate the proximal torque. All the torque and position signals at both pulleys were monitored by analog to digital conversion (ADC) modules and incremental encoder modules of the controller DS1104 and sent to the computer to record them for analysis.

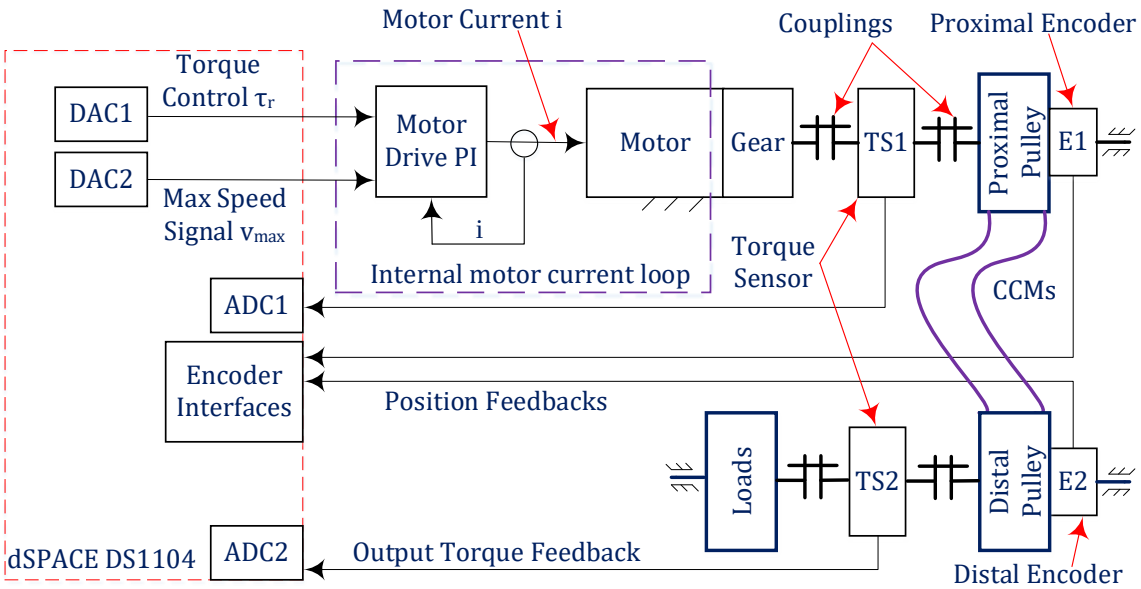

Fig. 3: The block diagram of the torque transmission investigation experiments

The recorded torque signals were filtered by a zero-phase digital filter in MATLAB (The MathWorks Inc., Natick, MA) to eliminate the high-frequency noises. The upper panel of Fig. 4 plots the data with respect to the recording time while the lower panel portrays the output torque $\tau_o(t)$ (measured by the distal torque sensor-TS2) with respect to the input torque $\tau_i(t)$ (measured by the proximal torque sensor-TS1). It is noticed that $\tau_o = \tau_d - (c_d\dot{\varphi}_d + J_d\ddot{\varphi}_d)$ and $\tau_i = \tau_p + (c_p\dot{\varphi}_p + J_p\ddot{\varphi}_p)$, where J_d, c_d, J_p, c_p are the inertial and viscous

coefficients at the distal and proximal pulleys. Denote τ_h as the total friction and hysteresis effects on the CCMs, one has $\tau_h(t) = \tau_i(t) - \tau_o(t)$.

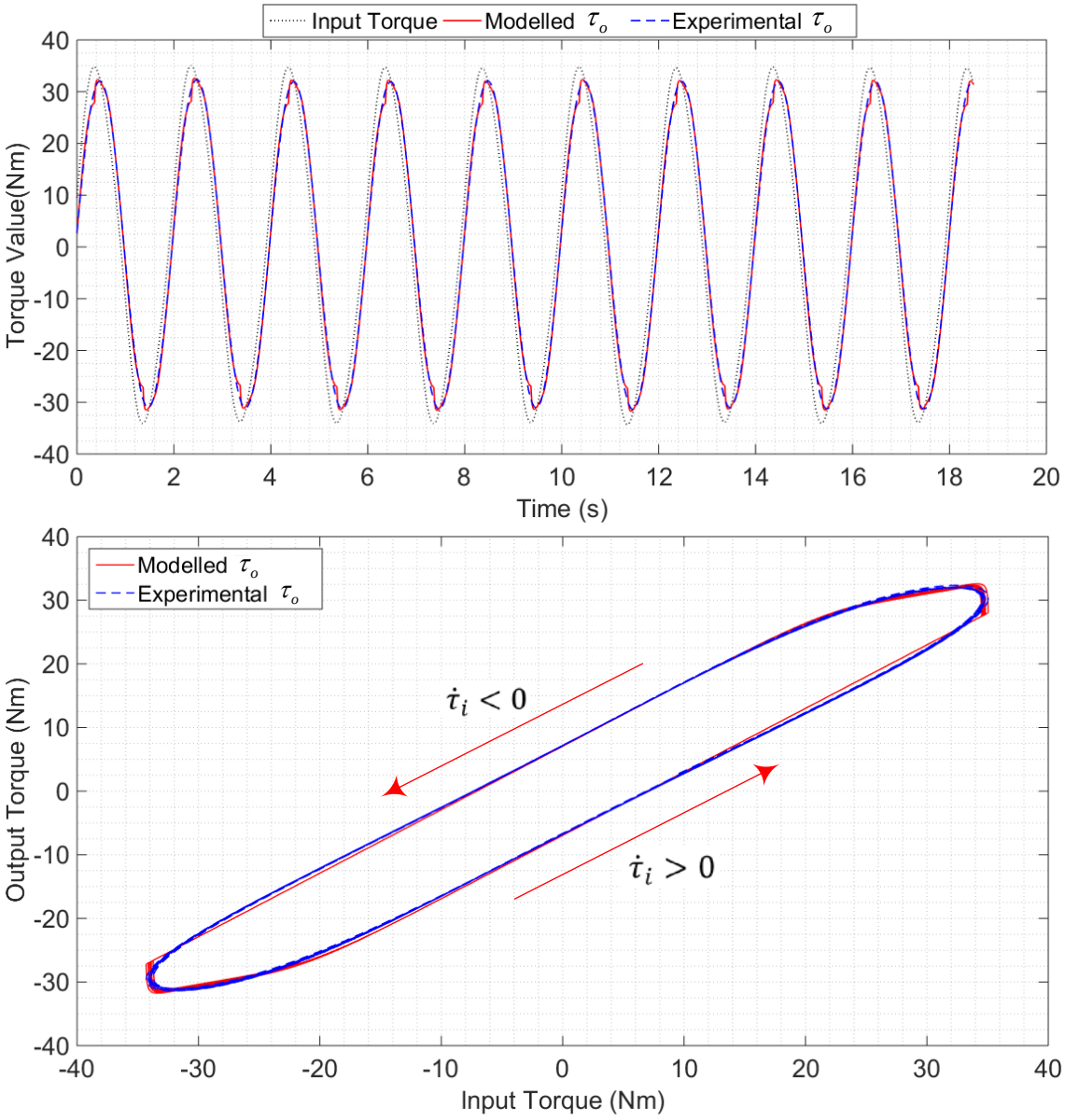

Fig. 4: Fitting of the observed experimental results and the simulation results (the Bouc-Wen model with torque input).

From the observed data of the torque transmission, we proposed using the Bouc-Wen model with torque input to portray the torque transmission profile (the dash line loop in the lower panel of Fig. 4) as follows

$$\tau_h = \kappa_\tau \tau_i + \kappa_\eta \eta + T_0 \tag{5}$$

$$\tau_o = \tau_i - \tau_h = B\tau_i - \kappa_\eta \eta - T_0, \tag{6}$$

in which $0 < \kappa_\tau, \kappa_\eta < 1$ represent the ratios between the system friction/hysteresis τ_h with the input toque τ_i and an internal state η; constant T_0 represents the effect of initial pretension. The relative ratio between output torque is defined as $B = 1 - \kappa_\tau > 0$. Also, the internal state η is derived by

$$\dot{\eta} = \rho[\dot{\tau}_i - \sigma|\dot{\tau}_i||\eta|^{n-1}\eta + (\sigma - 1)\dot{\tau}_i|\eta|^n]. \quad (7)$$

In this model, the input is the torque τ_i instead of the displacement, and $\dot{\tau}_i$ is the first time-derivative of τ_i. To evaluate the effectiveness of the Bouc-Wen model in describing the torque transmission, we adopted the Genetic Algorithm (GA) and the Nelder–Mead Simplex optimization methods to estimate the parameters of the model (5) - (7). The best estimated parameters will minimize the following fitness function

$$f(\rho, \sigma, n, B, \kappa_\eta, T_0) = \sqrt{\frac{1}{M}\sum_{i=1}^{M}\left(\tau_{om}(i) - \tau_o(i)\right)^2} \quad (8)$$

in which i is the sampling index, and M is the total number of recorded samples. This function is the root mean square error of the observed experimental output torque $\tau_o(i)$ and the estimated output torque $\tau_{om}(i)$. The value of $\tau_{om}(i)$ was approximated by using the Runge-Kutta fourth-order method and the estimated parameters, which were generated by the optimization methods. The GA method was used to roughly locate the global minimum of the fitness function and the Nelder-Mead simplex method refined the results subsequently. These optimization methods are supported in MATLAB. The lower panel in Fig. 4 also shows the modelled output torque τ_{om} (plotted by the continuous line) with the identified parameters: $\rho = 0.09582$, $\sigma = 98.36$, $n = 3.871$, $B = 0.9978$, $\kappa_\eta = 7.004$, and $T_0 = 0.05174$. The root mean square error is 0.6615 Nm (equivalent to 2.13 % of the range of the output torque). Also, other experimental trials with different cable-conduit curvature and cable pretension had been carried out for the same set of cable-conduit length and dimension as this set would be used for the ankle joint of the robotic foot. This was to assess the proposed model's effectiveness. Similar root mean square errors were observed during the identification process. For instance, another trial resulted: $\rho = 0.09353$, $\sigma = 62.49$, $n = 3.255$, $B = 0.9983$, $\kappa_\eta = 7.231$, $T_0 = 0.1272$, and $RMSE = 0.6424\ Nm$. It is obvious that the modelled output torque matches closely with the recorded output torque, therefore, we can use Bouc-Wen model to describe the torque transmission and compensate the hysteresis effects of the pair of CCMs. This modeling method avoids the dependence of friction on the proximal displacement and express the output distal torque directly in term of the proximal torque. With the support of a torque control mode from the servomotor and drive, the authors can calculate and generate a torque control signal directly for the actuator without the need for any conversion between the proximal displacement, acceleration, and moment. It is also noted that although the identification process has demonstrated the effectiveness of the Bouc-Wen hysteresis model in portraying the output torque versus input torque, the identified parameters depend on a specific configuration of the CCMs and may change with other configurations. Thus, the later parts of the paper will seek for an effective control method using Bouc-Wen model to compensate for hysteresis effects and improve control performance.

2.2.3 Torque Mode Control of the Brushless Servomotor

Base on the electrodynamic characteristics of the brushless servomotor, the servo drive, and the zero-backlash gearbox, one can express the torque measured by the proximal torque sensor as

$$\tau_i = N(\tau - J\ddot{\varphi} - \nu\dot{\varphi}) \tag{9}$$

$$\tau = Au_c \tag{10}$$

where τ is the generated motor torque, N is the gear ratio, and $-\nu\dot{\varphi}$, $-J\ddot{\varphi}$ are viscous and inertial effects on the servomotor and gearbox. $u_c(t)$ is the final torque control signal that the controller sends to the servo drive M701-03400100A, and A is a positive coefficient which depends on the servomotor and servo drive internal current proportional-integral (PI) loop.

3 Controller Design

Consider the external disturbance during the control progress and denote $y(t) = \tau_o(t)$ as the feedback output torque at the distal side of the CCMs, from Eq. (6), (9), and (10), one can write

$$y = \tau_o = BN(Au_c - J\ddot{\varphi} - \nu\dot{\varphi}) - \kappa_\eta\eta - T_0 = \alpha u_c - \vartheta_1 x_1 - \vartheta_2 x_2 - D_h, \tag{11}$$

$$D_h = \kappa_\eta\eta + d + T_0, \tag{12}$$

where $\alpha = BNA$, $\vartheta_1 = BN^2\nu$, $\vartheta_2 = BN^2J$ are positive constant parameters regarding the preset conditions of CCMs (e.g., the dimension and material of cables and conduits) and servomotor while $D_h(t)$ represents the total disturbance on system including the variable hysteresis effect $\kappa_\eta\eta$ on the CCMs (due to the variable curvature of the conduits), external disturbance $d(t)$, and the pretension offset torque T_0. Also, $x_1 = \dot{\varphi}_p$, $x_2 = \ddot{\varphi}_p$, and $\varphi = N\varphi_p$ are state variables (Note that φ_p is the angular displacement at the proximal pulley and φ is the angular displacement of the motor rotor). Denote $e(t)$ as the torque tracking error, one has

$$e(t) = y(t) - y_r(t). \tag{13}$$

Our goal is to design a closed-loop control scheme which can compensate the hysteresis effect and nonlinearities of the CCMs and enhance the torque tracking performance. This paper presents the design and experimental results of a new adaptive control scheme and three conventional closed-loop control schemes for this purpose. Only the stability of the new controller design is discussed. To be able to design such controllers, the following assumptions were made: (i) no cable slacking occurs during the experiments since sufficient pretension was established to the pair of CCMs; (ii) the reference torque profile $y_r(t)$ is explicit, piece-wise continuous, and bounded; (iii) the output torque feedback $y(t)$ and its first time-derivative $\dot{y}(t)$ are bounded.

3.1 Traditional Closed-loop Controllers

A closed-loop control signal can be calculated from three well-known and effective controllers PID, PI [47], and PIV [46, 48] as follows, respectively:

$$u_c(t) = -k_p e - k_i \int_0^t e(\omega)d\omega - k_d \dot{e} \tag{14}$$

$$u_c(t) = -k_p e - k_i \int_0^t e(\omega)d\omega \tag{15}$$

$$u_c(t) = -k_p e - k_i \int_0^t e(\omega)d\omega - k_d \dot{\varphi}_d \tag{16}$$

in which, $e(t)$ is the torque tracking error, $\int_0^t e(\omega)d\omega$ is the accumulation of error, $\dot{e}(t)$ is the changing speed of error, and $\dot{\varphi}_d$ is the angular velocity of the distal pulley.

3.2 New Robust Adaptive Controller

The above controllers are none-modeled controllers, which do not compensate for the hysteresis effects and disregard the nonlinear transmission characteristics of the system. To develop an adaptive control scheme, another assumption was made: (iv) the angular velocity and acceleration of the proximal pulley are assumed bounded. Then, we define the variable of interest as the accumulated error z, and the filtered tracking error s as follows

$$z = \int_{t_0}^t e(\omega)d\omega \tag{17}$$

$$s = \left(\frac{d}{dt} + \lambda\right) z = e + \lambda z \tag{18}$$

in which λ is an arbitrary positive constant. The integral lower limit t_0 can be chosen as the initial moment of the control process or the moment when e is at the proximity of zero. To derive the control signal u_c, we introduced the new virtual control signals $\bar{u}_c$ as follows

$$u_c = \hat{\beta}\bar{u}_c \tag{19}$$

in which $\hat{\beta}$ is the estimate of the new control coefficient $\beta = 1/\alpha$. Let $\tilde{\beta}$ be the estimated error of β as $\tilde{\beta} = \beta - \hat{\beta}$. From above definitions, the control term in (11) can be expressed in terms of the new virtual control signal $\bar{u}_c$ as follows

$$\alpha u_c = \alpha\hat{\beta}\bar{u}_c = \alpha\left(\beta - \tilde{\beta}\right)\bar{u}_c = \bar{u}_c - \alpha\tilde{\beta}\bar{u}_c \tag{20}$$

Then, the first time-derivatives of the accumulated error z and the new tracking error s defined by (13), (17), (18) and the closed-loop system are

$$\dot{z} = e = s - \lambda z \tag{21}$$

$$\dot{s} = \dot{e} + \lambda e = \dot{e} + \lambda(y - y_r) = \dot{e} + \lambda(\bar{u}_c - \alpha\tilde{\beta}\bar{u}_c - \vartheta_1 x_1 - \vartheta_2 x_2 - D_h - y_r) \tag{22}$$

Denote $\Delta_h > 0$ as the bound of the system disturbance $D_h(t)$ (i.e., $|D_h| \leq \Delta_h$), and denote $\hat{\vartheta}_i$ and $\widehat{\Delta}_h$ as the estimates of parameters ϑ_i and Δ_h, one has the corresponding estimated errors as $\tilde{\vartheta}_i = \vartheta_i - \hat{\vartheta}_i$, $\widetilde{\Delta}_h = \Delta_h - \widehat{\Delta}_h$. Then, the control and update laws can be designed as follows

$$\bar{u}_c = -ks + y_r - \frac{z + \dot{e}}{\lambda} + \hat{\vartheta}_1 x_1 + \hat{\vartheta}_2 x_2 - \widehat{\Delta}_h \tanh(s/\epsilon) \tag{23}$$

$$\dot{\hat{\beta}} = -\gamma\lambda s\bar{u}_c - \sigma_\alpha\hat{\beta} \tag{24}$$

$$\dot{\widehat{\Delta}}_h = \mu\lambda s \tanh(s/\epsilon) - \sigma\widehat{\Delta}_h \tag{25}$$

$$\dot{\hat{\vartheta}}_i = -\mu_i\lambda s x_i - \sigma_i\hat{\vartheta}_i \tag{26}$$

in which the arbitrary positive coefficient k denotes the control gain; and the positive parameters γ, μ, μ_i ($i = 1, 2$) represent the estimating coefficients. In addition, the leakage terms [49] introduced by the positive leakage coefficients σ_α, σ, and σ_i are added to the parameter estimated laws (24) - (26) to prevent parameter drifting. Moreover, the tangent hyperbolic function $\tanh(s/\epsilon)$ is used to replace the $sign(s)$ function as a smooth sign function, where ϵ is a small positive design constant.

Theorem 1: Consider the dynamic system, which is modeled by (6), (7), (11), (12) and satisfies the assumptions (i) - (iv), with the control and update laws (19), (21) - (26), the following statements hold.

i. All signals of the resulting closed-loop system are uniformly ultimately bounded.
ii. The filtered tracking error s and accumulated error z converge to a neighborhood of zero with the bound defined by $\delta = \sqrt{2\phi/\theta}$, where $\phi = \alpha\sigma_\alpha\beta^2/2\gamma + \sigma\Delta_h^2/2\mu + \sum_{i=1}^{2}(\sigma_i\vartheta_i^2/2\mu_i) + 0.2785\epsilon\lambda\Delta_h$ and $\theta = min(2\lambda, 2k\lambda, \sigma_1, \sigma_2, \sigma, \sigma_\alpha)$.
iii. The tracking error converges to a neighborhood of zero with the bound of $(1 + \lambda)\delta$.

Proof: Consider the Lyapunov function

$$V = \frac{1}{2}s^2 + \frac{1}{2}z^2 + \sum_{i=1}^{2}\frac{1}{2\mu_i}\tilde{\vartheta}_i^2 + \frac{1}{2\gamma}\alpha\tilde{\beta}^2 + \frac{1}{2\mu}\widetilde{\Delta}_h^2 \tag{27}$$

then, substitute (21), (22) into to the first time derivative of the Lyapunov function, one has

$$
\begin{aligned}
\dot{V} &= s\dot{s} + z\dot{z} + \sum_{i=1}^{2} \frac{\tilde{\vartheta}_i \dot{\tilde{\vartheta}}_i}{\mu_i} + \frac{\alpha\tilde{\beta}\dot{\tilde{\beta}}}{\gamma} + \frac{\tilde{\Delta}_h \dot{\tilde{\Delta}}_h}{\mu} = s\dot{s} + z(s - \lambda z) + \sum_{i=1}^{2} \frac{\tilde{\vartheta}_i \dot{\tilde{\vartheta}}_i}{\mu_i} + \frac{\alpha\tilde{\beta}\dot{\tilde{\beta}}}{\gamma} + \frac{\tilde{\Delta}_h \dot{\tilde{\Delta}}_h}{\mu} \\
&= -\lambda z^2 + s\left[z + \dot{e} + \lambda\left(\bar{u}_c - \alpha\tilde{\beta}\bar{u}_c - \vartheta_1 x_1 - \vartheta_2 x_2 - D_h - y_r\right)\right] - \sum_{i=1}^{2} \frac{\tilde{\vartheta}_i \dot{\tilde{\vartheta}}_i}{\mu_i} - \frac{\alpha\tilde{\beta}\dot{\tilde{\beta}}}{\gamma} - \frac{\tilde{\Delta}_h \dot{\tilde{\Delta}}_h}{\mu} \\
&= -\lambda z^2 + \lambda s\left[\bar{u}_c + \frac{z + \dot{e}}{\lambda} - \hat{\vartheta}_1 x_1 - \hat{\vartheta}_2 x_2 - y_r\right] - \frac{\tilde{\Delta}_h \dot{\tilde{\Delta}}_h}{\mu} - \lambda s D_h \\
&- \sum_{i=1}^{2} \tilde{\vartheta}_i \left(\lambda s x_i + \frac{\dot{\tilde{\vartheta}}_i}{\mu_i}\right) - \alpha\tilde{\beta}\left(\lambda s\bar{u}_c + \frac{\dot{\tilde{\beta}}}{\gamma}\right)
\end{aligned}
\tag{28}
$$

Substitute the control and update laws (23) - (26) into (28), one has

$$
\begin{aligned}
\dot{V} &= -\lambda z^2 + \lambda s\left[-ks - \hat{\Delta}_h \tanh\left(\frac{s}{\epsilon}\right)\right] + \sum_{i=1}^{2} \frac{\sigma_i \hat{\vartheta}_i \tilde{\vartheta}_i}{\mu_i} + \frac{\alpha\sigma_\alpha \hat{\beta}\tilde{\beta}}{\gamma} - \tilde{\Delta}_h \frac{\mu\lambda s \tanh\left(\frac{s}{\epsilon}\right) - \sigma\hat{\Delta}_h}{\mu} - \lambda s D_h \\
&\leq -\lambda z^2 - k\lambda s^2 + \sum_{i=1}^{2} \frac{\sigma_i \hat{\vartheta}_i \tilde{\vartheta}_i}{\mu_i} + \alpha \frac{\sigma_\alpha \hat{\beta}\tilde{\beta}}{\gamma} + \frac{\sigma\hat{\Delta}_h \tilde{\Delta}_h}{\mu} - \lambda s\left(\hat{\Delta}_h + \tilde{\Delta}_h\right)\tanh\left(\frac{s}{\epsilon}\right) + \lambda|s|\Delta_h
\end{aligned}
\tag{29}
$$

The inequality (29) was obtained from the fact that $|D_h| \leq \Delta_h$, and therefore $-\lambda s D_h \leq \lambda|s|\Delta_h$. Subsequently, by adopting the inequality $0 \leq |s| - s\tanh(s/\epsilon) \leq 0.2785\epsilon$, which was introduced by *Lemma 1* in [50], one has $0 \leq \lambda\Delta_h[|s| - s\tanh(s/\epsilon)] \leq 0.2785\epsilon\lambda\Delta_h$. Hence, the inequality (29) becomes

$$
\dot{V} \leq -\lambda z^2 - k\lambda s^2 + \frac{\alpha\sigma_\alpha}{\gamma}\hat{\beta}\tilde{\beta} + \frac{\sigma}{\mu}\hat{\Delta}_h\tilde{\Delta}_h + \sum_{i=1}^{2} \frac{\sigma_i}{\mu_i}\hat{\vartheta}_i\tilde{\vartheta}_i + 0.2785\epsilon\lambda\Delta_h \tag{30}
$$

In addition, the first leakage term in (30) can be rewritten as follows

$$
\begin{aligned}
\frac{\alpha\sigma_\alpha}{\gamma}\hat{\beta}\tilde{\beta} &= \frac{\alpha\sigma_\alpha}{\gamma}\tilde{\beta}\left(\beta - \tilde{\beta}\right) = \frac{\alpha\sigma_\alpha}{\gamma}\left(\beta\tilde{\beta} - \tilde{\beta}^2\right) = \frac{\alpha\sigma_\alpha}{\gamma}\left[-\frac{\tilde{\beta}^2}{2} - \frac{1}{2}\left(\tilde{\beta}^2 - 2\beta\tilde{\beta} + \beta^2\right) + \frac{\beta^2}{2}\right] \\
&= \frac{\alpha\sigma_\alpha}{\gamma}\left[-\frac{\tilde{\beta}^2}{2} - \frac{1}{2}\left(\tilde{\beta} - \beta\right)^2 + \frac{\beta^2}{2}\right] \leq -\sigma_\alpha\frac{\alpha\tilde{\beta}^2}{2\gamma} + \frac{\alpha\sigma_\alpha\beta^2}{2\gamma}
\end{aligned}
\tag{31}
$$

Similarly, one can obtain

$$
\frac{\sigma}{\mu}\hat{\Delta}_h\tilde{\Delta}_h \leq -\sigma\frac{\tilde{\Delta}_h^2}{2\mu} + \frac{\sigma\Delta_h^2}{2\mu} \tag{32}
$$

$$
\sum_{i=1}^{2} \frac{\sigma_i}{\mu_i}\hat{\vartheta}_i\tilde{\vartheta}_i \leq -\sum_{i=1}^{2} \sigma_i \frac{\tilde{\vartheta}_i^2}{2\mu_i} + \sum_{i=1}^{2} \frac{\sigma_i\vartheta_i^2}{2\mu_i} \tag{33}
$$

Hence, the time derivative of the Lyapunov function becomes

$$
\begin{aligned}
\dot{V} &\leq -2\lambda\frac{z^2}{2} - 2k\lambda\frac{s^2}{2} - \sum_{i=1}^{2} \sigma_i \frac{\tilde{\vartheta}_i^2}{2\mu_i} - \sigma_\alpha\frac{\alpha\tilde{\beta}^2}{2\gamma} - \sigma\frac{\tilde{\Delta}_h^2}{2\mu} + \frac{\alpha\sigma_\alpha\beta^2}{2\gamma} + \frac{\sigma\Delta_h^2}{2\mu} + \sum_{i=1}^{2} \frac{\sigma_i\vartheta_i^2}{2\mu_i} + 0.2785\epsilon\lambda\Delta_h \\
&\leq -\theta V + \phi
\end{aligned}
\tag{34}
$$

if one denote $\theta = min(2\lambda, 2k\lambda, \sigma_1, \sigma_2, \sigma, \sigma_\alpha)$and the constant quantity $\phi = \alpha\sigma_\alpha\beta^2/2\gamma + \sigma\Delta_h^2/2\mu + \sum_{i=1}^{2}(\sigma_i\vartheta_i^2/2\mu_i) + 0.2785\epsilon\lambda\Delta_h$. Hence, when $V \geq V^* = \phi/\theta$,$\dot{V} \leq 0$, which implies that V is a non-increasing function. Therefore, from the definition of Lyapunov function in (27), all tracking errors z, s, and estimated errors $\tilde{\Delta}_h$, $\tilde{\beta}$, and $\tilde{\vartheta}_i(i = 1, 2)$ are bounded. Thus, the corresponding estimates $\hat{\Delta}_h$, $\hat{\beta}$, and $\hat{\vartheta}_i(i = 1, 2)$ are also bounded. These combine with assumptions (ii) - (iv) and control laws (26), (30) to make the control signals $\bar{u}_c$ and u_c be bounded. Then, (24) - (26) imply that $\dot{\hat{\beta}}$, $\dot{\hat{\Delta}}_h$, $\dot{\hat{\vartheta}}_i$ are bounded.

Furthermore, multiply both sides of (34) with $e^{\theta t}$ and then integrate the inequality, one can obtain

$$0 \leq \frac{1}{2}z^2 \leq V(t) \leq \left[V(t_0) - \frac{\phi}{\theta}\right]e^{-\theta(t-t_0)} + \frac{\phi}{\theta} \tag{35}$$

in which $V(t_0)$ is obtained at the initial moment t_0 when the errors are zero

$$V(t_0) = \frac{1}{2\gamma}\alpha\tilde{\beta}^2(t_0) + \frac{1}{2\mu}\tilde{\Delta}_h^2(t_0) + \sum_{i=1}^{2}\frac{1}{2\mu_i}\tilde{\vartheta}_i^2(t_0) \tag{36}$$

Thus, one has

$$|z| \leq \sqrt{2\left[V(t_0) - \frac{\phi}{\theta}\right]e^{-\theta(t-t_0)} + \frac{2\phi}{\theta}} \tag{37}$$

When t increases, $[V(t_0) - \phi/\theta]e^{-\theta(t-t_0)} \to 0$, implying that the accumulated error z converges to the proximity of zero with the bound δ as $|z| \leq \delta = \sqrt{2\phi/\theta}$. Using a similar analysis procedure, one can obtain the bound of the filtered tracking error as $|s| \leq \delta = \sqrt{2\phi/\theta}$. This implies statements (ii). Then, from the inequality $|s| = |e + \lambda z| \geq |e| - |\lambda z|$, one can prove statement (iii) as

$$|e| \leq |e + \lambda z| + \lambda|z| = |s| + \lambda|z| \leq \delta + \lambda\delta = (1 + \lambda)\delta \tag{38}$$

Since the bounds are independent of t_0, all signals are uniformly ultimately bounded and statement (i) holds.

■

Remark 1: The leakage terms in the adaptive laws (24) - (26) prevent the estimated parameters drifting to infinity and the use of the $\tanh(.)$ function helps the system avoid chattering, therefore, they help the system achieve robustness. On the other hand, they also introduce a residue of the tracking error. Thus, to achieve smaller error, one may choose very small values for σ_i, ,σ, σ_α, and ϵ. However, too small leakage terms cannot adapt with a steep increase of the estimated values. If certain knowledge of the parameter limit is available, one can employ the switching σ-modification leakage terms [49] to improve the control performance.

Remark 2: The noise effects containing in the time derivative of error $\dot{e}$ can be minimized by increasing the error accumulation gain λ. In addition, the higher values of the control and update gains k, λ, γ, μ, μ_i can mitigate the effect of the initial estimated errors and increase the adaptation speed. However, the large gains

can cause chattering and high amplitude tracking error. In practice, one can choose reasonable values of k and λ with respect to the reference y_r and the amplitude of $\dot{e}$, subsequently, one should fix these gains to adjust the estimating gains.

4 Experiment Setup and Validation

4.1 Experimental Procedure

While Fig. 1 illustrates the system working principles, Fig. 5 shows the real experimental model and Fig. 6 sketches the common block diagram for all four mentioned control schemes. All aforementioned control algorithms were implemented and compiled in the MATLAB-Simulink environment. The result programs were loaded into the dSPACE controller's software and hardware (i.e., the Control Desk and the DS1104 board) thereafter. In operation, the controller DS1104 receives the feedback signals from the distal torque sensor and encoders to calculate control signals. Two control signals are sent to the servo drive via 16-bit-DAC modules. The torque signal commands the drive and motor to generate the required torque while the maximum speed signal is used to limit the rotating speed of the motor.

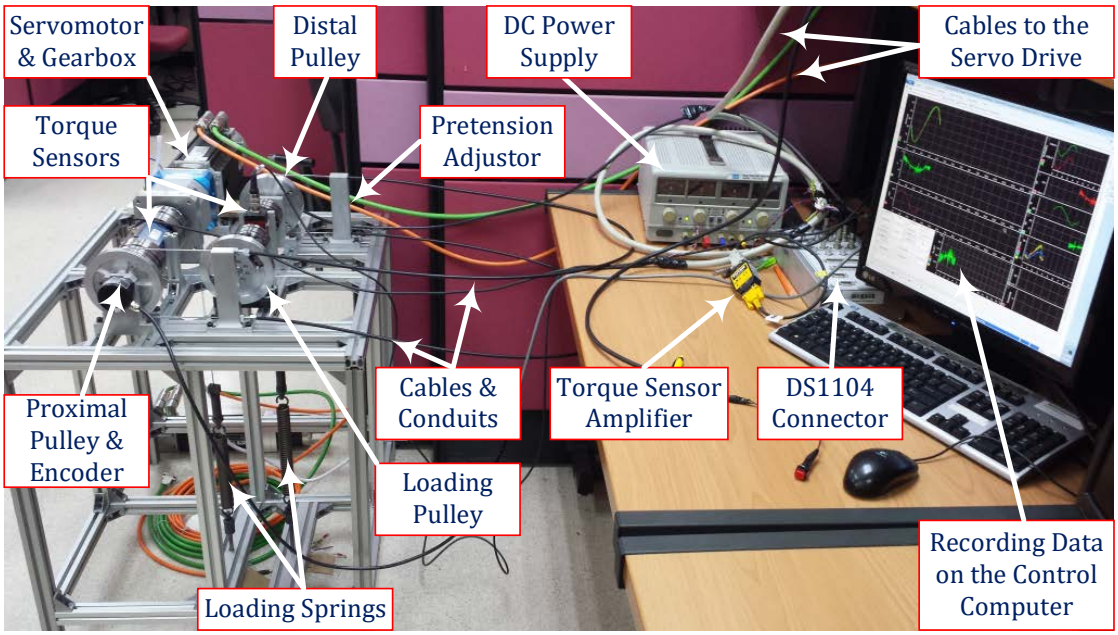

Fig. 5: The real experimental system

In addition, while the PI and PID controllers merely use the output torque feedback to calculate the control signals, the PIV controller also utilizes the angular velocity of the distal pulley (fed back by the distal encoder). On the other hand, the adaptive control law employs the rotating speed and acceleration of the proximal pulley to estimate and compensate the viscous and inertial effects of the actuator.

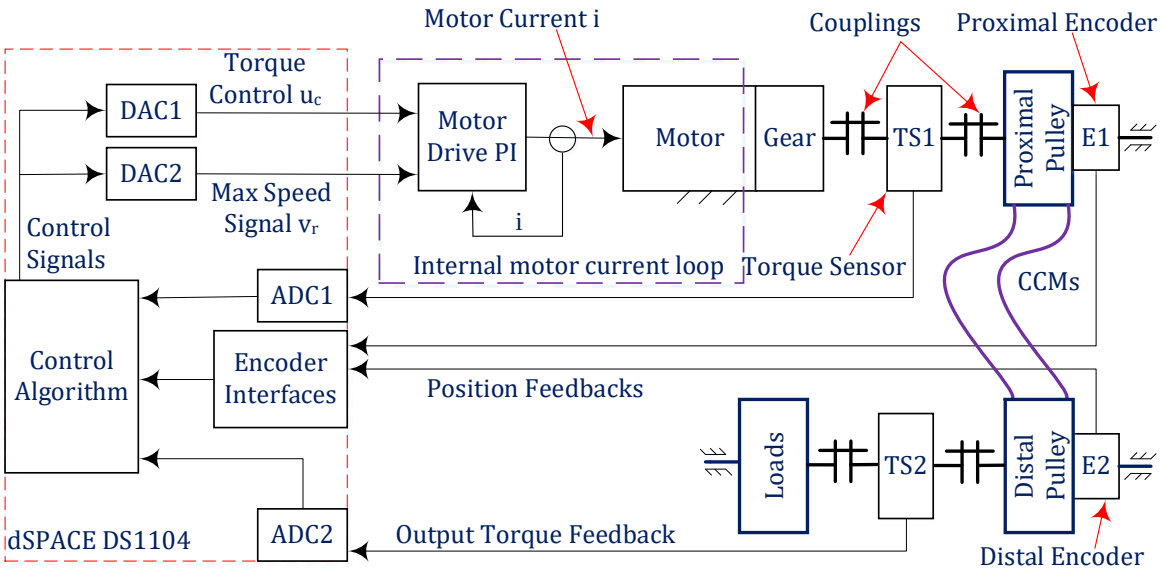

Fig. 6: The common block diagram for all closed-loop torque tracking control schemes

4.2 Experimental Results

To evaluate the performance of the aforementioned schemes, two types of experiments were conducted: control with fixed and randomly varying configurations of the CCMs. A combination of two sinusoidal signals (Signal A has an amplitude of 10 Nm and a frequency of 0.25 Hz, and Signal B has an amplitude of 3 Nm and a frequency of $0.2\sqrt{3}$ Hz) was used as the torque reference $y_r(t)$. Fig. 7 shows the results of the control experiments with fixed cable-conduit configurations using the four control schemes. Specifically, the torque tracking data of the PI, PID, PIV, and adaptive control schemes are plotted respectively from the top. For each scheme, the left panel shows the same reference signal $25 + 10\sin(2\pi t \times 0.25) + 3\sin(2\pi t \times 0.2\sqrt{3})$ (Nm) and the corresponding output torque (Nm) while the middle panel plots the torque tracking error (Nm) at the same scale with the left panel. On the other hand, the right panel plots the corresponding torques (Nm) at the proximal and distal pulleys at a larger scale. Apparently, the proximal torque has much larger values and its graph fluctuates more wildly than the distal torque. All horizontal axes represent the trial time in second. The chosen parameters of the conventional controllers are shown in Table 1 while the designed parameters of the adaptive controller are shown in Table 2. The initial guesses for parameter integrations are $\widehat{\Delta}_{h0} = 7$, $\hat{\beta}_0 = 0$, and $\hat{\vartheta}_{i0} = 0$.

Table 1: The designed parameters for PI, PID, and PIV controllers

Designed Parameters	k_p	k_i	k_d
PI Controller	30	18	–
PID Controller	30	18	2
PIV Controller	30	18	10

Table 2: Designed Parameters for the Adaptive Controller

Parameters	k	λ	$\lambda\mu$	$\lambda\gamma$	$\lambda\mu_i$	σ	σ_α	σ_i	ϵ
Values	24	8	0.05	0.002	0.004	0.01	0.01	0.01	0.05

It is obvious that the torque tracking error of the adaptive controller has much smaller amplitudes compared to the other tracking errors. The root mean square error (RMSE) of the PI, PID, and PIV control trials are about two folds of RMSE of the adaptive compensation trials. Quantitatively, Table 3 shows the RMSE of six typical trials of four control schemes in both fixed and varying configuration conditions. The average, standard deviation and percentage to the maximum reference of these errors are also calculated and summarized. For the fixed configuration of CCMs, the adaptive scheme has the RMSE of 0.3027 ± 0.0081 (Nm), which is approximate 0.8% of the maximum reference, while the RMSEs of the PI, PID, and PIV tracking trials are 0.5991 ± 0.0154 (Nm), 0.6093 ± 0.0164 (Nm), and 0.532 ± 0.0134 (Nm) respectively. Also, the graph of the adaptive compensation error is very consistent while the others have significant fluctuations especially when the system reverses its direction. This is because the adaptive scheme, which is aided by the model-based compensation term $-\widehat{\Delta}\tanh(s/\epsilon)$, can mitigate the hysteresis effects and keep the output torque track closely to the sudden reverses of the reference. In addition, it can be also observed that the PI controller, which does not include the damping term $-k_d\dot{e}$, shows more significant chattering responses than the PID and PIV controllers. Furthermore, the PIV controller shows better tracking performance compared to the PID controller. This is resulted from the fact that the PID controller uses the derivative of the torque tracking error for the damping term while the PIV controller takes the angular speed of the output pulley to compensate for the fluctuation. The output torque, which is fed back by the ADC module, usually contains more noise than the output angular displacement, which is monitored by the incremental encoder. Incremental encoders can introduce noise due to their discrete nature. Its output may contain wrong signals due to mechanism vibration or electronic noise. However, modern encoders are built with differential signals and shielded cable to deal with electronic noise. The experimental system is quite stable with a minimum vibration of the encoder shaft. Thus, the output position of high-resolution incremental encoders usually contains less noise than the ADC signals from strain gauge components of the torque sensor. The strain gauge output is more likely affected by mechanical vibrations even with small-amplitude vibration. The analog signal is also easier affected by electronic noise from the motor windings and switching circuit or the strong electromagnetic field round the 3-phases AC servomotor. The ADC signal may also contain more noise from the quantization (i.e., sampling) process. Consequently, the damper composed by the output angular speed works more efficiently. Thus, the average RMSE of the PIV control tracking trials is slightly smaller than the PI and PID control trials (about 0.5 Nm compared to about 0.6 Nm).

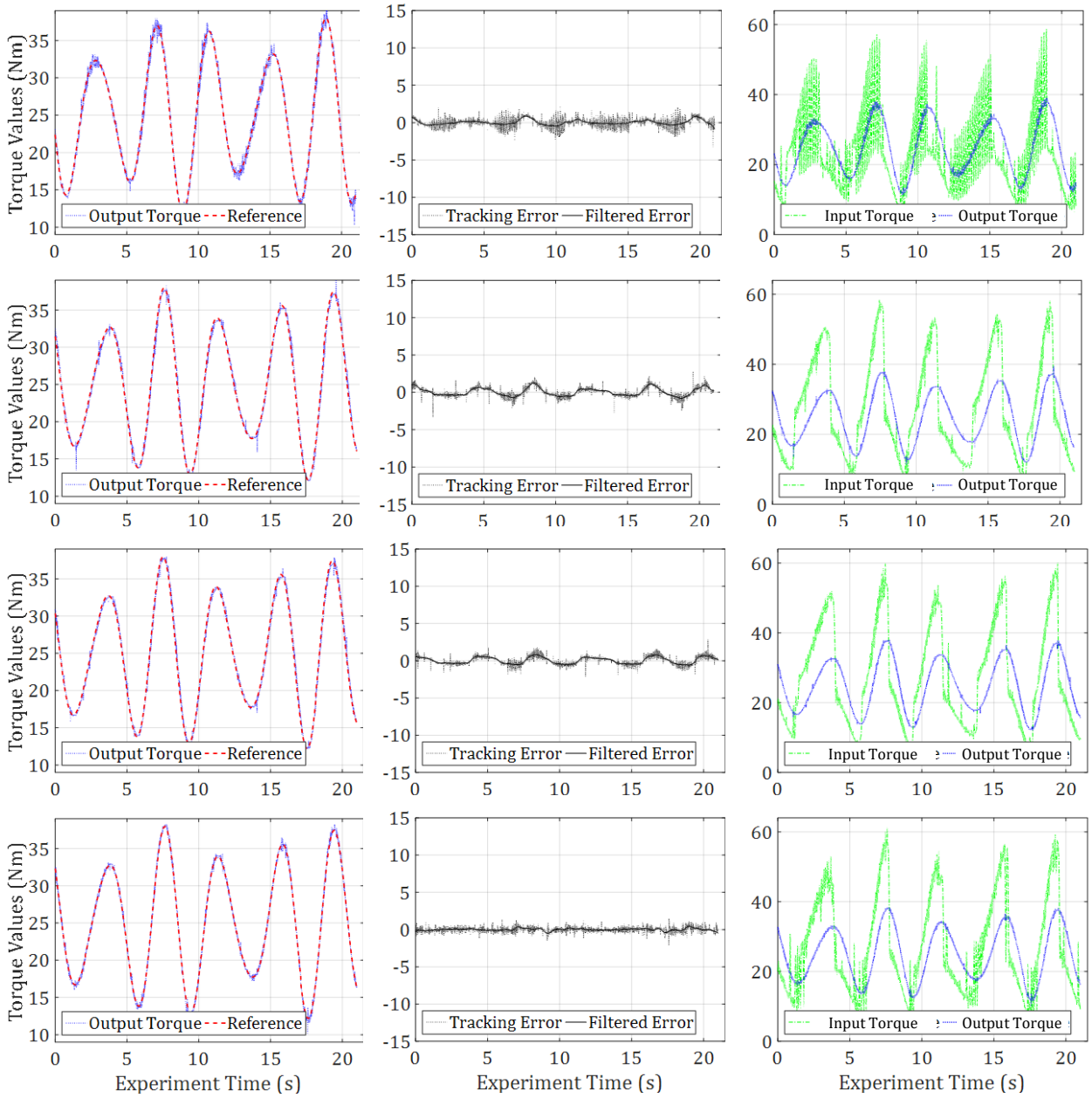

Fig. 7: The experimental results of four closed-loop control schemes for the same reference signal $25 + 10sin(2\pi t \times 0.25) + 3sin(2\pi t \times 0.2\sqrt{3})$ (Nm) when the cable-conduit configurations were fixed. The tracking performance of the PI, PID, PIV and adaptive control schemes are shown respectively from top to bottom. The left panels plot the reference and output torques, the middle panels show the corresponding tracking errors and the right panels compare the torque values at the proximal and distal pulley.

To validate the effectiveness of the designed control schemes in coping with the nature change of the cable conduit configuration, other control trials were carried out with varying configurations of the CCMs. To be able to compare the results with the fixed CCMs' configuration trials, the same controllers' parameters were used for torque tracking with the same reference signal. However, during the experiments with varying CCMs configuration, the authors manually moved the pair of conduits to fluctuate their routes. The conduit routes were moved randomly in all three directions up-down, back-front, and left-right to change their routes as

much as possible (within the limits to not cause any cable folding). Fig. 8 shows the result data for these varying configuration experiments. The left panels plot the output torques for the same reference signal $25 + 10\sin(2\pi t \times 0.25) + 3\sin(2\pi t \times 0.2\sqrt{3})$ (Nm) of the PI, PID, PIV, and adaptive control schemes respectively; the right panels show the corresponding tracking errors. The quantitative results of these experimental trials are also shown in the second part of Table 3. It can be observed that similar results had been recorded. The adaptive control scheme still shows more consistently effective capability in output torque tracking. The data in Table 3 also demonstrate that tracking error of trials with varying CCM configurations are minor larger than those with the fixed CCM configurations.

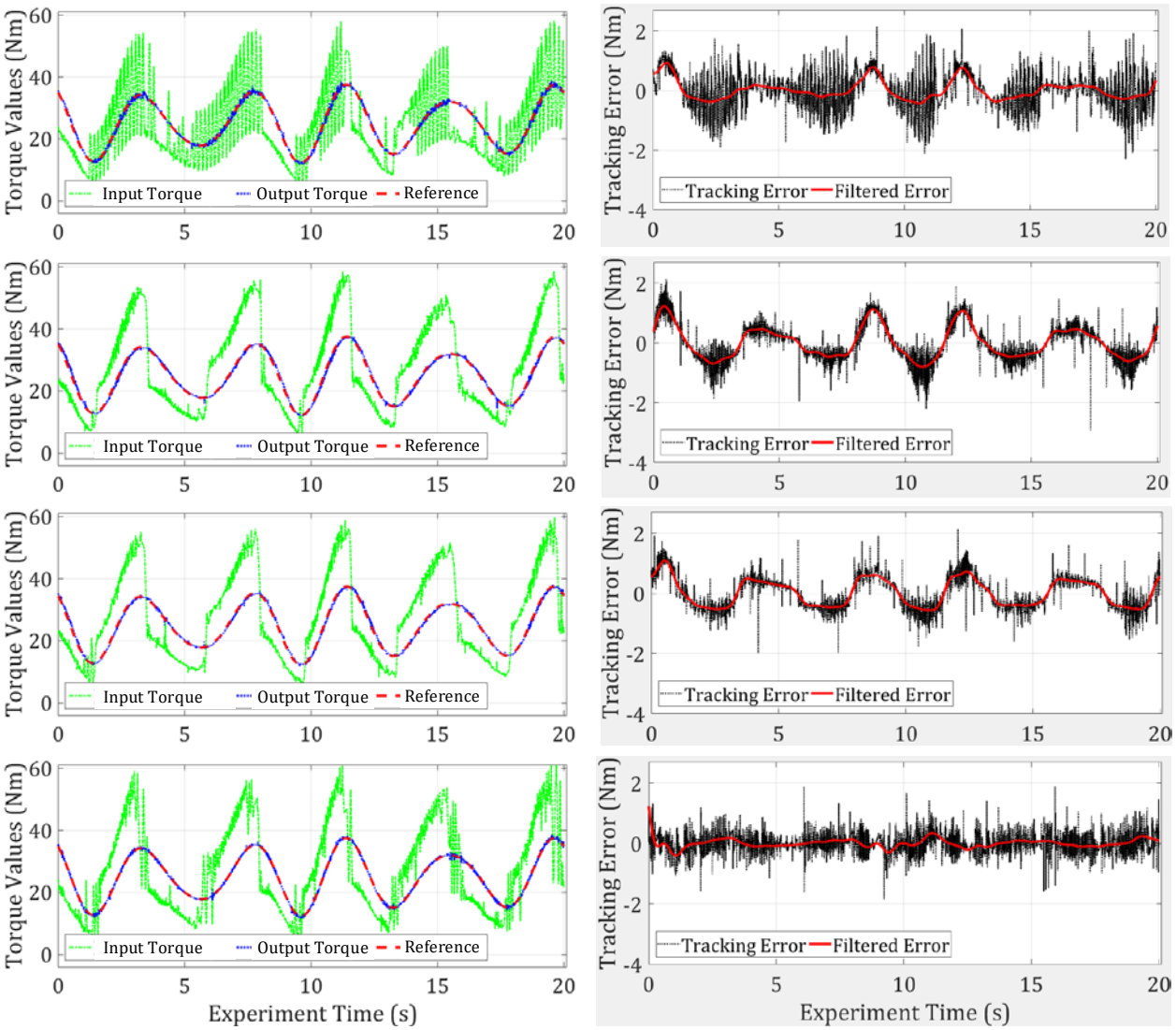

Fig. 8: The experimental results of four closed-loop control schemes for the same reference signal $25 + 10sin(2\pi t \times 0.25) + 3sin(2\pi t \times 0.2\sqrt{3})$ (Nm) when the cable-conduit configurations were varying during the trials. The tracking performance of the PI, PID, PIV, and adaptive control schemes are shown respectively from top to bottom. The left panels plot the reference and output torques and the middle panels show the corresponding tracking errors.

Table 3: The root mean square error (RMSE) of the experimental trials of four control schemes in both fixed and varying configurations of the CCMs. The results of six typical trials for each scheme are described.

	Fixed Configuration				Varying Configuration			
Trials	PI	PID	PIV	Adaptive	PI	PID	PIV	Adaptive
1	0.5967	0.6323	0.5550	0.2937	0.6368	0.6333	0.5375	0.3005
2	0.5856	0.5960	0.5212	0.2915	0.6054	0.5912	0.5468	0.3112
3	0.6087	0.6058	0.5296	0.3045	0.6071	0.6052	0.5164	0.3242
4	0.5942	0.6271	0.5403	0.3084	0.5905	0.6262	0.5577	0.3213
5	0.6250	0.5942	0.5243	0.3091	0.5901	0.6187	0.5269	0.3247
6	0.5845	0.6004	0.5213	0.3092	0.5902	0.6090	0.5084	0.3350
Average	0.5991	0.6093	0.532	0.3027	0.6034	0.6139	0.5323	0.3195
SD	0.0154	0.0164	0.0134	0.0081	0.0182	0.0153	0.0186	0.012
% to Max	1.5766	1.6034	1.4	0.7966	1.5879	1.6155	1.4008	0.8408

To evaluate the transient performance, we plot the recorded signals in a shorter time interval (12 seconds) at the initial control processes in Fig. 9. All control schemes were initiated at the same moment of the same interval of the reference signal $25 + 10sin(2\pi t \times 0.25) + 3sin(2\pi t \times 0.2\sqrt{3})$ (Nm). It is clear that the robust adaptive control scheme performs slower convergent performance due to the effects of initial estimates, but its torque tracking performance was enhanced significantly after the adaptation took effect. It can be observed that the PI controller, which is not supported by a damping component perform poorer capability in coping with fluctuation while PID and PIV which are supported by a damping term can extinguish the fluctuation effectively. Three conventional control schemes perform similar capabilities at the initiation. At that moment, adaptive control has larger fluctuation because the parameters had not converged to their real values yet. However, after the adaptation took effects, the adaptive control shows significant better performance with consistently smaller tracking error as shown in the right panels. Fig. 10 plots the convergence processes of the four estimated parameters $\hat{\beta}$, $\hat{\Delta}$, $\hat{\vartheta}_1$, and $\hat{\vartheta}_2$.

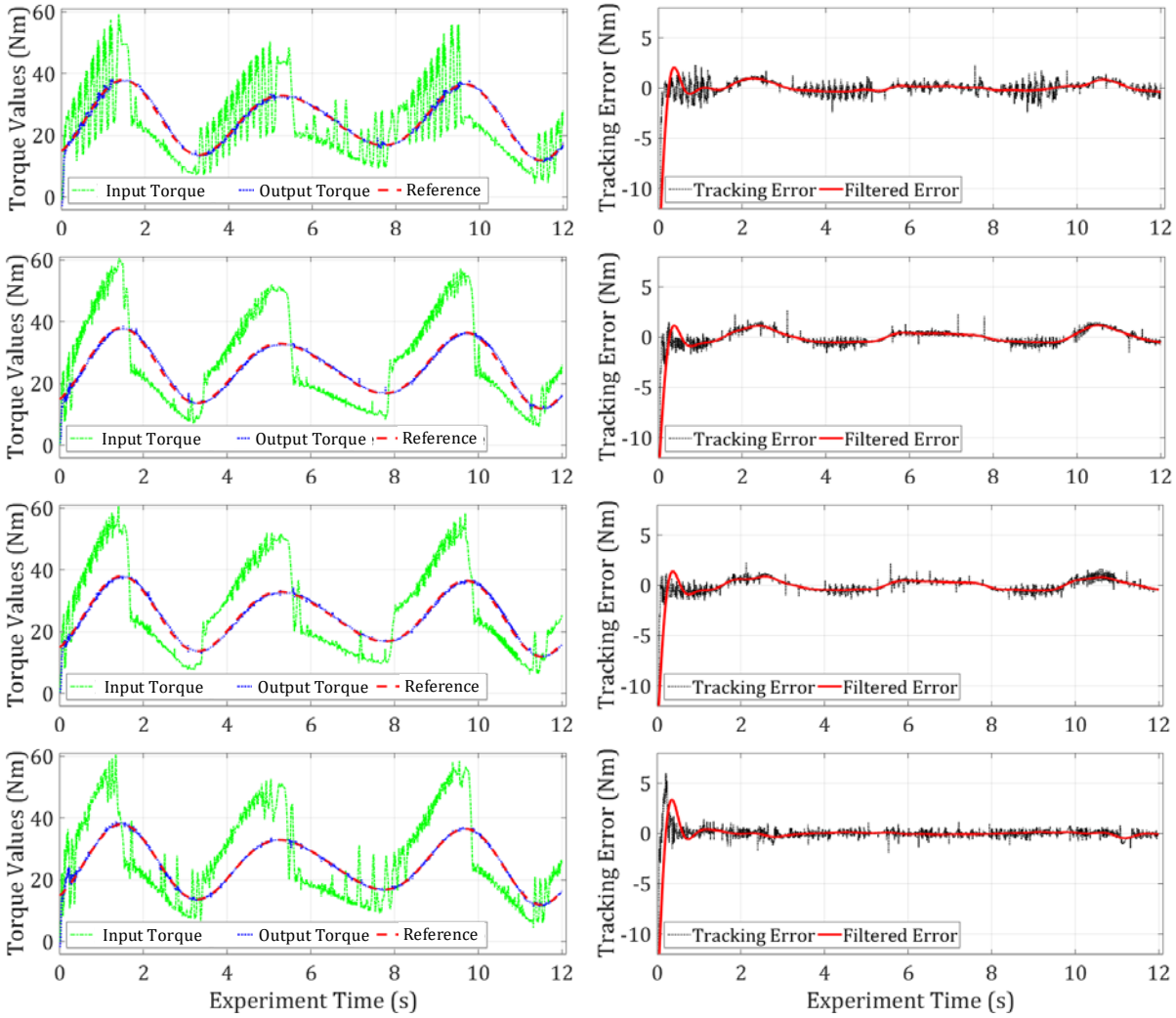

Fig. 9: Transient performance of the four closed-loop control schemes for the same reference signal $25 + 10sin(2\pi t \times 0.25) + 3sin(2\pi t \times 0.2\sqrt{3})$ (Nm) when the control trials initiate. The results of the PI, PID, PIV, and adaptive schemes are shown respectively from top to bottom. The left panels show the reference, output and proximal torques, the right panels plot the corresponding tracking errors.

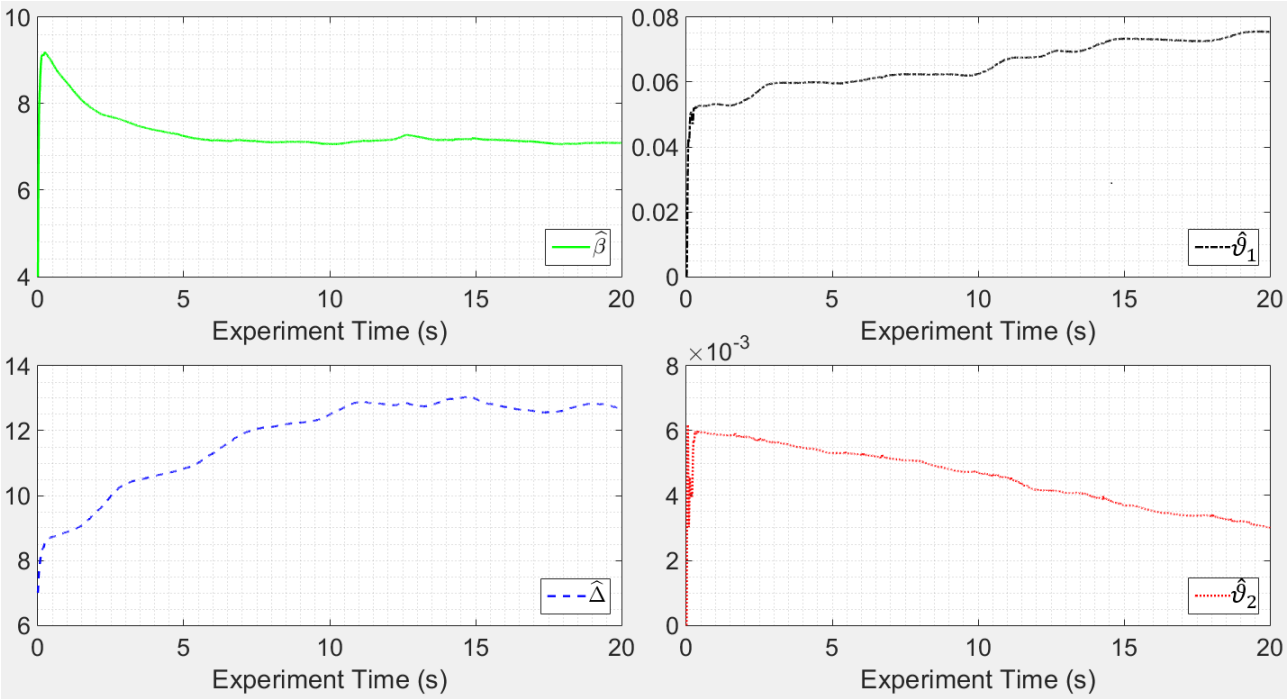

Fig. 10: The convergence of estimating parameters

5 Discussion and Conclusion

This paper proposed a new approach for output torque tracking control for the systems preceded by CCMs. With the availability of torque feedback, four closed-loop control schemes were designed and implemented to control a 1-DOF system actuated by a pair of CCMs. Direct torque signals were generated by the controllers and sent to a servo drive operating in torque control modes to adjust the motor output torque. Although all control schemes performed effectively, the new adaptive control scheme utilized the Bouc-Wen hysteresis model to estimate and compensate for the bound of hysteresis and disturbance effects and therefore provided better results. The Bouc-Wen model used the proximal torque as the input signal of the hysteresis profile instead of the proximal displacement as in the original Bouc-Wen model and other modeling approaches. By expressing the output torque in terms of the input torque, this model enabled a possibility for a new adaptive controller to estimate and compensate for the disturbance and hysteresis effects on the CCMs. It also estimated and compensated for the dynamic viscous and inertial effects on the high-speed rotating rotor and the gearbox. This adaptive compensation scheme did not require in advance the value of the model parameters. All unknown parameters such as the bound of total disturbance and hysteresis effects, the viscous and inertial coefficients of the motor and gearbox, and the control gain were online estimated during the control trials.

The stability of the new control scheme was discussed in detail and experiments has been carried out to validate its effectiveness. It significantly enhanced the torque tracking performance for the system preceded by a pair of CCMs in both fixed and varying configurations of the CCMs. In addition, for the traditional

controller, the D term contains the derivative from tracking error *e*, thus, it is usually very sensitive with disturbance and noise. Especially, the feedback signal in this paper is an analog-to-digital conversion (ADC) signal of the output torque. This ADC signal contains noise from high frequency sampling rate, and strain gauge component of the torque sensor is also affected by the strong electromagnetic field around the 3-phase AC servomotor and drive due to their switching circuit activity. Thus, if the derivative of this ADC signal combines with a high D gain, the control signal will cause excessive response and overshoot. However, with a certain value of D gain, the D term will reduce overshoot of the system. In the experimental results, the lack of a D term or a V term in the PI controller made the system fluctuate, but the PID and PIV performed well in reducing this overshoot and thus stabilized the system.

For future developments, experimental validation with full-scale loading (compared to the robotic footwear testing system) will be conducted. Subsequently, these control schemes will be developed and implemented for control the robotic foot for footwear testing with the availability of output torque feedbacks. The footwear testing system is equipped with multiple load cells at the contact floor to monitor the ground reaction forces and calculate the real time torque of the foot's joints.

REFERENCE

[1] D. J. Abbott, C. Becke, R. I. Rothstein, and W. J. Peine, "Design of an endoluminal NOTES robotic system," in *2007 IEEE/RSJ International Conference on Intelligent Robots and Systems*, 2007, pp. 410-416.

[2] G. W. Dachs and W. J. Peine, "A Novel Surgical Robot Design: Minimizing the Operating Envelope Within the Sterile Field," in *Engineering in Medicine and Biology Society, 2006. EMBS '06. 28th Annual International Conference of the IEEE*, 2006, pp. 1505-1508.

[3] S. J. Phee, "Master and slave transluminal endoscopic robot (MASTER) for natural orifice transluminal endoscopic surgery (NOTES)," presented at the 31st Annual International Conference of the IEEE EMBS, Minneapolis, Minnesota, USA, 2009.

[4] W. Xu, H. K. Leung, P. W. Y. Chiu, and C. C. Y. Poon, "A feed-forward friction compensation motion controller for a tendon-sheath-driven flexible robotic gripper," in *2013 IEEE International Conference on Robotics and Biomimetics, ROBIO 2013*, 2013, pp. 2112-2117.

[5] G. Palli, G. Borghesan, and ClaudioMelchiorri, "Modeling, Identification, and Control of Tendon-Based Actuation Systems," *IEEE TRANSACTIONS ON ROBOTICS,* vol. 28, 2012.

[6] K. Kong, "Proxy-based impedance control of a cable-driven assistive system," *Mechatronics,* vol. 23, pp. 147-153, 2013.

[7] A. T. Asbeck, S. M. M. De Rossi, I. Galiana, Y. Ding, and C. J. Walsh, "Stronger, smarter, softer: Next-generation wearable robots," *IEEE Robotics and Automation Magazine,* vol. 21, pp. 22-33, 2014.

[8] A. T. Asbeck, K. Schmidt, and C. J. Walsh, "Soft exosuit for hip assistance," *Robotics and Autonomous Systems,* vol. 73, pp. 102-110, 11// 2015.

[9] A. T. Asbeck, K. Schmidt, I. Galiana, D. Wagner, and C. J. Walsh, "Multi-joint soft exosuit for gait assistance," in *Robotics and Automation (ICRA), 2015 IEEE International Conference on*, 2015, pp. 6197-6204.

[10] F. Zhang, L. Hua, Y. Fu, H. Chen, and S. Wang, "Design and development of a hand exoskeleton for rehabilitation of hand injuries," *Mechanism and Machine Theory,* vol. 73, pp. 103-116, 3// 2014.

[11] J. F. Veneman, "A Series Elastic- and Bowden-Cable-Based Actuation System for Use as Torque Actuator in Exoskeleton-Type Robots," *The International Journal of Robotics Research,* vol. 25, pp. 261-281, 2006.

[12] T. Lenzi, N. Vitiello, S. M. M. D. Rossi, S. Roccella, F. Vecchi, and M. C. Carrozza, "NEUROExos- A variable impedance powered elbow exoskeleton," presented at the IEEE International Conference on Robotics and Automation, Shanghai, China, 2011.

[13] J. M. Caputo and S. H. Collins, "A universal ankle-foot prosthesis emulator for human locomotion experiments," *Journal of Biomechanical Engineering,* vol. 136, 2014.

[14] T. L. Nguyen, S. J. Allen, and S. J. Phee, "Exploiting 3D printing technology to develop robotic running foot for footwear testing," *Virtual and Physical Prototyping,* vol. 8, pp. 259-269, 2013.

[15] T. L. Nguyen, T. N. Do, M. W. S. Lau, and S. J. Phee, "Modelling, design, and control of a robotic running for footwear testing with flexible actuator," in *1st International Conference in Sports Science Technology (ICSST)*, Singapore, 2014, pp. 505–514.

[16] D. J. Stefanyshyn and B. M. Nigg, "Mechanical energy contribution of the metatarsophalangeal joint to running and sprinting," *Journal of Biomechanics,* vol. 30, pp. 1081-1085, 1997.

[17] T. F. Novacheck, "The biomechanics of running," *Gait & Posture,* vol. 7, pp. 77-95, 1// 1998.

[18] P. O. Riley, J. Dicharry, J. Franz, U. Della Croce, R. P. Wilder, and D. C. Kerrigan, "A kinematics and kinetic comparison of overground and treadmill running," *Med Sci Sports Exerc,* vol. 40, pp. 1093-100, Jun 2008.

[19] B. Brackx, M. Van, A. Matthys, B. Vanderborght, and D. Lefeber, "Passive Ankle-Foot Prosthesis Prototype with Extended Push-Off," *International Journal of Advanced Robotic Systems,* p. 1, 2013.

[20] B. E. Lawson, H. A. Varol, and M. Goldfarb, "Standing stability enhancement with an intelligent powered transfemoral prosthesis," *IEEE Transactions on Biomedical Engineering,* vol. 58, pp. 2617-2624, 2011.

[21] S. K. Au, J. Weber, and H. Herr, "Powered ankle-foot prosthesis improves walking metabolic economy," *IEEE Transactions on Robotics,* vol. 25, pp. 51-66, 2009.

[22] F. Sup, H. A. Varol, J. Mitchell, T. Withrow, and M. Goldfarb, "Design and control of an active electrical knee and ankle prosthesis," in *Proceedings of the 2nd Biennial IEEE/RAS-EMBS International Conference on Biomedical Robotics and Biomechatronics, BioRob 2008*, 2008, pp. 523-528.

[23] F. Tian and X. Wang, "The Design of a Tendon-Sheath-Driven Robot," in *Mechatronics and Machine Vision in Practice, 2008. M2VIP 2008. 15th International Conference on*, 2008, pp. 280-284.

[24] S. J. Phee, S. C. Low, P. Dario, and A. Menciassi, "Tendon sheath analysis for estimation of distal end force and elongation for sensorless distal end," *Robotica,* vol. 28, pp. 1073-1082, 2010.

[25] L. Chen, X. Wang, and W. L. Xu, "Inverse Transmission Model and Compensation Control of a Single-Tendon–Sheath Actuator," *IEEE TRANSACTIONS ON INDUSTRIAL ELECTRONICS,* vol. 61, 2014.

[26] Q. Wu, X. Wang, L. Chen, and F. Du, "Transmission Model and Compensation Control of Double-Tendon-Sheath Actuation System," *IEEE Transactions on Industrial Electronics,* vol. 62, pp. 1599-1609, 2015.

[27] V. Agrawal, W. J. Peine, and B. Yao, "Modeling of transmission characteristics across a cable-conduit system," *IEEE Transactions on Robotics,* vol. 26, pp. 914-924, 2010.

[28] S. B. Kesner and R. D. Howe, "Position Control of Motion Compensation Cardiac Catheters," *Robotics, IEEE Transactions on,* vol. 27, pp. 1045-1055, 2011.

[29] R. Reilink, S. Stramigioli, and S. Misra, "Image-based hysteresis reduction for the control of flexible endoscopic instruments," *Mechatronics,* vol. 23, pp. 652-658, 9// 2013.

[30] T. N. Do, T. Tjahjowidodo, M. W. S. Lau, T. Yamamoto, and S. J. Phee, "Hysteresis modeling and position control of tendon-sheath mechanism in flexible endoscopic systems," *Mechatronics,* vol. 24, pp. 12-22, 2// 2014.

[31] T. N. Do, T. Tjahjowidodo, M. W. S. Lau, and S. J. Phee, "Nonlinear friction modelling and compensation control of hysteresis phenomena for a pair of tendon-sheath actuated surgical robots," *Mechanical Systems and Signal Processing,* vol. 60–61, pp. 770-784, 8// 2015.

[32] M. Kaneko, W. Paetsch, and H. Tolle, "Input-Dependent Stability of Joint Torque Control of Tendon-Driven Robot Hands," *IEEE Transactions on Industrial Electronics,* vol. 39, pp. 96-104, 1992.

[33] U. Jeong and K. J. Cho, "Feedforward friction compensation of Bowden-cable transmission via loop routing," in *IEEE International Conference on Intelligent Robots and Systems*, 2015, pp. 5948-5953.

[34] T. N. Do, T. Tjahjowidodo, M. W. S. Lau, and S. J. Phee, "Adaptive control for enhancing tracking performances of flexible tendon–sheath mechanism in natural orifice transluminal endoscopic surgery (NOTES)," *Mechatronics,* vol. 28, pp. 67-78, 6// 2015.

[35] T. N. Do, T. Tjahjowidodo, M. W. S. Lau, and S. J. Phee, "Position Control of Asymmetric Nonlinearities for a Cable-Conduit Mechanism," *IEEE Transactions on Automation Science and Engineering,* 2015.

[36] T. N. Do, T. Tjahjowidodo, M. W. S. Lau, and S. J. Phee, "Real-time enhancement of tracking performances for cable-conduit mechanisms-driven flexible robots," *Robotics and Computer-Integrated Manufacturing,* vol. 37, pp. 197-207, 2// 2016.

[37] F. Ikhouane and J. Rodellar, *Systems with Hysteresis: Analysis, Identification and Control using the Bouc-Wen Model*: John Wiley & Sons, 2007.

[38] M. Ismail, F. Ikhouane, and J. Rodellar, "The hysteresis Bouc-Wen model, a survey," *Archives of Computational Methods in Engineering,* vol. 16, pp. 161-188, 2009.

[39] J. Zhou, C. Wen, and Y. Zhang, "Adaptive backstepping control of a class of uncertain nonlinear systems with unknown backlash-like hysteresis," *IEEE Transactions on Automatic Control,* vol. 49, pp. 1751-1759, 2004.

[40] J. Zhou, C. Wen, and T. Li, "Adaptive output feedback control of uncertain nonlinear systems with hysteresis nonlinearity," *IEEE Transactions on Automatic Control,* vol. 57, pp. 2627-2633, 2012.

[41] C. Y. Su, Y. Stepanenko, J. Svoboda, and T. P. Leung, "Robust adaptive control of a class of nonlinear systems with unknown backlash-like hysteresis," *IEEE Transactions on Automatic Control*, vol. 45, pp. 2427-2432, 2000..

[42] J. Cai, C. Wen, H. Su, and Z. Liu, "Robust adaptive failure compensation of hysteretic actuators for a class of uncertain nonlinear systems," *IEEE Transactions on Automatic Control*, vol. 58, pp. 2388-2394, 2013.

[43] Z. Li, C. Y. Su, and T. Chai, "Compensation of hysteresis nonlinearity in magnetostrictive actuators with inverse multiplicative structure for preisach model," *IEEE Transactions on Automation Science and Engineering,* vol. 11, pp. 613-619, 2014.

[44] K. Kong, J. Bae, and M. Tomizuka, "Torque mode control of a cable-driven actuating system by sensor fusion," *Journal of Dynamic Systems, Measurement and Control, Transactions of the ASME,* vol. 135, 2013.

[45] J. Lu, K. Haninger, W. Chen, and M. Tomizuka, "Design and torque-mode control of a cable-driven rotary series elastic actuator for subject-robot interaction," in *2015 IEEE International Conference on Advanced Intelligent Mechatronics (AIM)*, 2015, pp. 158-164.

[46] J. Zhang, C. C. Cheah, and S. H. Collins, "Experimental comparison of torque control methods on an ankle exoskeleton during human walking," in *Proceedings - IEEE International Conference on Robotics and Automation*, 2015, pp. 5584-5589.

[47] K. J. Astrom, "PID Controllers: Theory, Design, and Tuning," *The International Society of Measurement and Control,* 1995 1995.

[48] M. Takegaki and S. Arimoto, "A New Feedback Method for Dynamic Control of Manipulators," *Journal of Dynamic Systems, Measurement, and Control,* vol. 103, pp. 119-125, 1981.

[49] P. A. Ioannou and J. Sun, *Robust adaptive control*: Courier Corporation, 2012.

[50] M. M. Polycarpou, "Stable adaptive neural control scheme for nonlinear systems," *Automatic Control, IEEE Transactions on,* vol. 41, pp. 447-451, 1996.